Reliability Engineering and System Safety 278 (2027) 113747



Contents lists available at ScienceDirect

Reliability Engineering and System Safety

journal homepage: www.elsevier.com/locate/ress



A satellite-based framework for resilience assessment of railway embankments

Mengyi Wang [a], Hongrui Wang [a], Alfredo Núñez [a,*], Bart De Schutter [b]

[a] Section of Railway Engineering, Delft University of Technology, Delft, 2628CN, The Netherlands
[b] Delft Center for Systems and Control, Delft University of Technology, 2628 CD, Delft, The Netherlands

ARTICLE INFO

Keywords:
Railway infrastructure
Resilience assessment
Insar
Deformation monitoring
Reconstruction uncertainty

ABSTRACT

Understanding how railway infrastructures degrade and respond to disturbances is essential for assessing their performance and resilience over time. Such behavior can be inferred from satellite-observed deformation, which provides wide spatial coverage and frequent observations. However, translating satellite-observed deformation into quantitative resilience assessment of railway infrastructure performance remains challenging under incomplete viewing geometries and associated uncertainties.

This paper proposes a satellite-based framework for assessing railway embankment resilience, using deformation patterns as observable proxies for changes in embankment-related railway performance. A reconstruction strategy integrates complementary satellite viewing geometries to recover missing observations and estimate two-dimensional deformation time series with associated uncertainties.

Two deformation-based indicators relevant to resilience assessment are developed: a multi-year indicator characterizing performance stability over the full observation period, and an event-based indicator characterizing deformation changes a posteriori around independently identified disturbance events. The framework is evaluated against independent track geometry (TG) measurements in a case study. The multi-year deformation indicator shows a significant association with deterioration in the Track Quality Index. For the event-based indicator, an elevated-TG response was observed in 61.0% of alarm InSAR cases, whereas no elevated TG response was observed in 74.9% of stable InSAR cases. In this case study, these results indicate that satellite-derived deformation indicators can provide a higher-frequency complement to conventional railway embankment assessment.

1. Introduction

Climate change and increasing climate variability [1-3] have intensified the frequency and magnitude of extreme hydrological events, posing growing challenges to the safety and durability of civil infrastructure [4]. In soft-soil areas, engineering structures are particularly vulnerable to both multi-year consolidation-induced settlement and short-term hydrologically driven disturbances [5,6], leading to differential deformation. In this regard, resilience, broadly defined as the ability of an engineering system to withstand disturbances and to recover its functionality, has received increasing attention in infrastructure monitoring [7,8]. Quantifying resilience across both multi-year and event-based time scales is therefore essential for understanding infrastructure behaviors under evolving environmental conditions.

Railway infrastructure is sensitive to ground deformation [9]. Multi-year differential settlement may progressively degrade track geometry [10,11], leading to increased maintenance requirements, speed restrictions, and even safety risks. At the same time, hydrological disturbances associated with extreme changes in moisture conditions, such as extreme rainfall events [12,13], can induce transient deformation responses or accelerate existing settlement, potentially triggering abrupt deterioration. Both cumulative deformation and event-related responses may therefore influence railway performance and safety.

To monitor and assess railway deformation, in situ track geometry (TG) inspections [14,15] are widely used, while satellite-based Interferometric Synthetic Aperture Radar (InSAR) techniques [16-18] have been adopted as a complementary monitoring source. TG provides direct indicators of railway condition, whereas InSAR enables spatially distributed retrospective characterization of embankment settlement

* Corresponding author.
E-mail address: a.a.nunezvicencio@tudelft.nl (A. Núñez).

https://doi.org/10.1016/j.ress.2026.113747
Received 11 May 2026; Received in revised form 30 September 2026; Accepted 27 October 2026
Available online 28 October 2026
0951-8320/© 2026 The Authors. Published by Elsevier Ltd. This is an open access article under the CC BY license (http://creativecommons.org/licenses/by/4.0/).

[19,20] and deformation trends [21]. Historical maintenance records have also been used to retrospectively identify and characterize climate-related railway infrastructure failures [22]. However, comparatively limited attention has been given to interpreting historical deformation during identified disturbance periods, particularly in the context of resilience-oriented assessment.

Therefore, this paper proposes an a posteriori satellite-based framework that extends deformation monitoring toward deformation-related resilience assessment of railway embankments. It evaluates historical deformation around identified hydrological disturbance events alongside performance stability over the full multi-year observation period, aiming to address the following overarching question: how can incomplete multi-geometry InSAR observations be reconstructed into two-dimensional deformation time series to support multi-year and event-based assessment, and to what extent are the resulting indicators consistent with deterioration derived from independent track-geometry measurements? Specifically, this paper contributes to the state of the art in the field as follows:

(1) Develops a satellite-based framework enabling deformation-related resilience assessment of railway embankments under incomplete and uncertain InSAR observations.
(2) Proposes a railway adaptive grid and a feature-weighted Dynamic Time Warping (DTW)-based reconstruction strategy to recover missing multi-orbit satellite observations.
(3) Introduces a Reconstruction Consistency Index (RCI) for quality screening and control of reconstruction-related uncertainty.
(4) Develops InSAR-derived indicators to characterize multi-year differential settlement and assess deformation responses around identified hydrological disturbances.
(5) Assesses the consistency of the proposed indicators with independent track-geometry deterioration data in a case study in the Netherlands.

The remainder of the paper is as follows. Section 2 presents the methodology, covering time-series reconstruction, reconstruction consistency screening, and the development of multi-year and event-based indicators. Section 3 presents the case study and the associated datasets used for analysis. Section 4 presents the results of deformation-based resilience assessment and discussion. Finally, Section 5 concludes the paper.

2. Methodology

As illustrated in Fig. 1, the proposed framework consists of four main components. First, Level-2 InSAR measurements serve as the essential data sources for the proposed approach. Second, the InSAR observations are organized using a railway-oriented adaptive grid developed in this paper to structure the data along the railway. Third, a segment-based reconstruction strategy is applied to recover missing multi-orbit observations by combining deformation time-series segmentation with feature-weighted DTW-based donor-receptor matching. The reconstructed observations are subsequently used for Line-of-Sight (LOS) decomposition to retrieve two-dimensional deformation components, and the RCI is introduced to characterize reconstruction consistency and to limit the influence of reconstruction-related uncertainty. Finally, the reconstructed deformation series are translated into two deformation-based indicators relevant to resilience assessment: a multi-year indicator of spatially heterogeneous settlement as a proxy for performance stability, and an event-based indicator of deformation changes around independently identified hydrological disturbances as a proxy for disturbance response. Their engineering relevance is further examined through an indirect consistency assessment with track-geometry deterioration data in the case study.

2.1. InSAR data foundation

InSAR observations provide one-dimensional displacements in the satellite's LOS direction. Since the actual ground deformation is 3D, this LOS measurement represents a projection of motion components [23] and therefore requires decomposition to retrieve ground deformation. The relationship between the LOS displacement and the three-dimensional ground motion components [16] can be expressed as:

$$d_{\mathrm{LOS}} = \begin{bmatrix} -\sin\theta\cos\alpha & \sin\theta\sin\alpha & \cos\theta \end{bmatrix} \begin{bmatrix} d_{\mathrm{e}} \\ d_{\mathrm{n}} \\ d_{\mathrm{u}} \end{bmatrix} \tag{1}$$

where θ is the local incidence angle (the angle between the local zenith and the looking vector of the satellite), α is the satellite heading, and d_{e}, d_{n}, and d_{u} are the east-west, north-south, and up-down components of motion, respectively.

Ascending and descending InSAR observations provide only two independent LOS equations for three displacement components, making the full three-dimensional inversion underdetermined. Moreover,

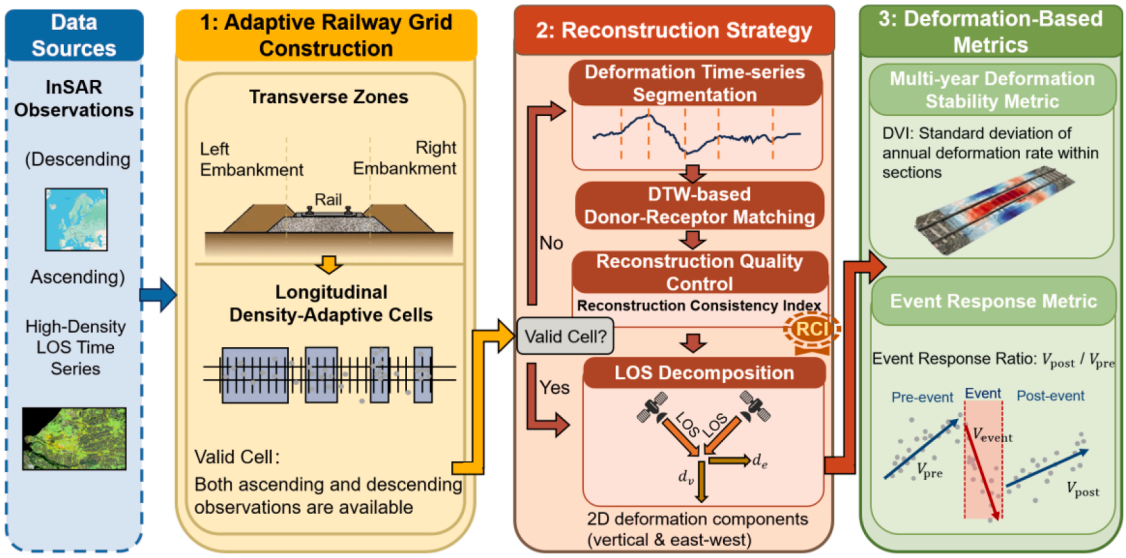


Fig. 1. Overview of the proposed framework.

because of the near-polar orbit configuration of Sentinel-1, the observations have limited sensitivity to north-south motion [24]. Therefore, when the direction is predominantly oriented parallel to the north, it is reasonable to assume that no appreciable displacement occurs in the north-south direction [5,25]. In this paper, the railway is mainly parallel to the north direction. Moreover, the dominant deformation is expected to consist of vertical settlement and lateral movement induced by train loading, whereas deformation along the railway is expected to be relatively small. Accordingly, the north-south displacement component is assumed to be negligible, allowing the vertical and east-west displacement components to be estimated from the ascending and descending LOS observations:

$$\begin{bmatrix} d_u \\ d_e \end{bmatrix} = \begin{bmatrix} \cos\theta_{asc} & -\sin\theta_{asc}\cos\alpha_{asc} \\ \cos\theta_{desc} & -\sin\theta_{desc}\cos\alpha_{desc} \end{bmatrix}^{-1} \begin{bmatrix} d_{asc} \\ d_{desc} \end{bmatrix} \quad (2)$$

To support this decomposition, the input observations must be spatially organized into railway-oriented cells containing both ascending and descending viewing geometries. However, the heterogeneous distribution of InSAR measurement points means that this requirement is not always satisfied. The following sections therefore introduce an adaptive railway grid to organize the observations and a reconstruction strategy to recover missing orbital time series.

2.2. Adaptive railway grid construction

Based on the observation requirements described in Section 2.1, an adaptive railway grid is developed to organize ascending and descending InSAR measurements into spatial cells suitable for two-dimensional deformation decomposition. Grid-based spatial organization is commonly adopted in InSAR monitoring to structure deformation observations [26]. However, a uniform grid may fail to capture spatial heterogeneity in deformation behavior along linear infrastructures [27,28]. To address this limitation in railway monitoring, a transverse partitioning strategy is developed to distinguish functional zones across the railway line. More specifically, the railway is divided into two functional zones: the rail and the embankments. Let C denote the railway centerline and let $d(p_i, C)$ represent the perpendicular distance from measurement point p_i to C. Here, W_{rail} denotes the half-width of the rail-core zone, measured from the centerline to its lateral boundary, while W_{emb} denotes the maximum transverse extent of the embankment from the centerline, with $W_{emb} > W_{rail}$. Points satisfying $|d(p_i, C)| \leq W_{rail}$ are classified as belonging to the rail, whereas points satisfying $W_{rail} < |d(p_i, C)| \leq W_{emb}$ are classified as embankment points. This classification enables function-specific monitoring and interpretation of deformation behavior across different structural zones of the railway.

Given the spatial heterogeneity of InSAR measurement point distributions [27], a density-adaptive longitudinal partitioning strategy is developed to define the cell length along the railway alignment. Each cell represents the basic spatial unit for deformation analysis, and its length L is adaptively determined based on the local availability of observations. To preserve spatial resolution, the cell length is constrained by an upper bound L_{max}. Starting from a minimum cell length L_{min}, the cell length is progressively adjusted according to the local density of InSAR measurement points. If the required observational constraints cannot be satisfied within the limit of L_{max}, the corresponding cell is labeled as an invalid cell.

To ensure reliable two-dimensional deformation decomposition, each cell must contain observations from both ascending and descending satellite orbits [16]. In summary, as shown in Fig. 2, the integration of transverse partitioning and density-adaptive longitudinal segmentation results in a structured representation of the railway corridor, consisting of three functional strips (left embankment, rail core, and right embankment) further subdivided into a grid of rectangular cells with variable lengths. This adaptive railway grid ensures that each valid cell contains sufficient observations from both viewing geometries to support stable and accurate deformation decomposition, while preserving the spatial resolution permitted by the local data density.

2.3. Reconstruction strategy

2.3.1. Deformation time-series segmentation

Despite the adaptive partitioning, the heterogeneous spatial distribution of InSAR measurement points leaves some cells with observations from only one viewing geometry. A time-series reconstruction strategy is therefore developed to recover the missing orbital observations by exploiting temporal similarities among cells. To enable similarity-based matching between deformation time series [29], representative features describing their temporal behavior need to be extracted [30]. However, raw deformation time series derived from InSAR measurements often contain noise [31], which may affect the subsequent feature extraction and similarity matching. Several methods have been proposed for time-series denoising and trend extraction, including moving-average smoothing, wavelet-based filtering, and model-based decomposition techniques [32].

However, LOESS smoothing [33] is sensitive to the choice of window

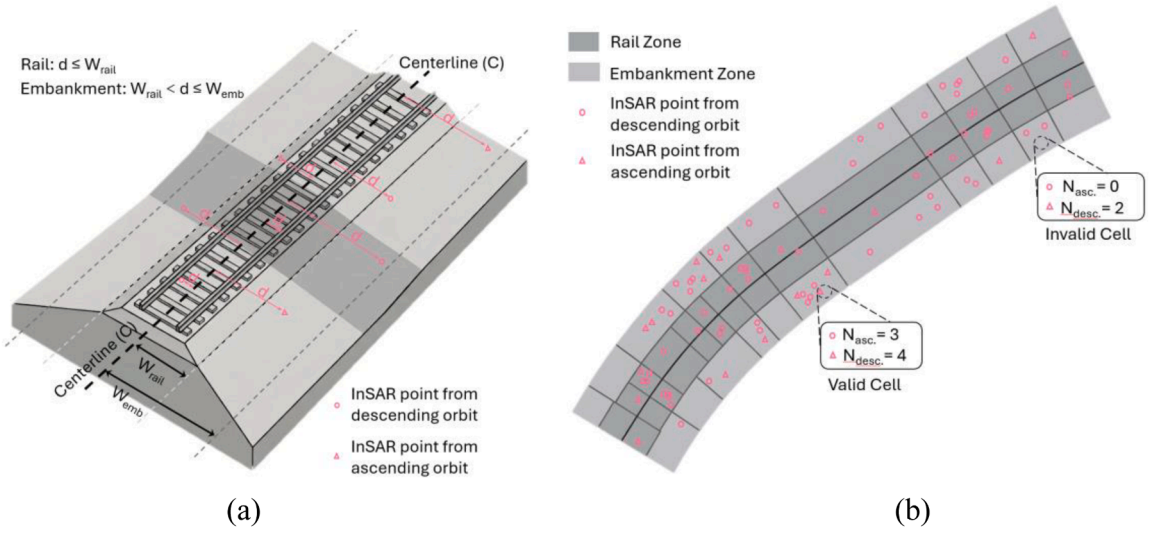


Fig. 2. Schematic illustration of the adaptive grid-based partitioning of the railway: (a) transverse division into three functional strips, and (b) resulting grid of density-adaptive rectangular cells.

size and may lead to over-smoothing of multi-year deformation trends, while seasonal-trend decomposition methods such as STL [34] are primarily designed for time series with clear periodic patterns, which are generally absent in InSAR deformation data. Because railway embankment deformation generally consists of a slowly varying long-term component superimposed with shorter-term fluctuations, a method capable of separating these components without assuming periodicity is required. To obtain a stable representation of such deformation behavior, the Hodrick-Prescott (HP) filter [35,36] is adopted to decompose the deformation signal into a smooth trend component and a residual component. The trend component captures the multi-year deformation evolution, while the residual component represents event-based variations and local disturbances.

After HP filtering, a polynomial function [37] is fitted to the extracted trend series to provide a continuous functional representation required for the subsequent reconstruction of the deformation process. The HP smoothing parameter (λ) controls the smoothness of the extracted trend: a smaller λ allows the trend to follow fluctuations more closely, whereas a larger λ produces a smoother trend component. The polynomial degree (p) determines the flexibility of the fitted curve, with a higher degree allowing more complex nonlinear deformation patterns to be represented. Since λ affects the trend extracted from the original time series and p further controls the shape of the fitted curve, these two parameters jointly influence the subsequent reconstruction process.

The inflection points of the fitted curve are then used to divide the trend series into multiple temporal segments representing different stages of deformation behavior. Instead of using fixed segmentation, segment boundaries were automatically determined from the sign changes of the second derivative of the fitted polynomial curve. This strategy allows the segmentation to be driven by curvature changes in the deformation trend, rather than by predefined time windows or a fixed number of segments. For cells with limited deformation variability, this avoids unnecessary over-segmentation. For cells affected by deformation events or complex nonlinear variations, it can preserve stage information related to acceleration, deceleration, and trend transitions.

Statistical indicators are calculated within each cell. In particular, the mean velocity (μ_{vel}) and mean acceleration (μ_{acc}) are used to quantify the deformation rate and its variation, while the residual RMSE (σ_{res}) reflects the magnitude of local deviations between the original series and the fitted trend. By transforming deformation time series into segmentation-wise representation, the proposed approach captures both global deformation trends and local dynamic variations.

2.3.2. DTW-based donor-receptor matching

Building upon the feature extraction within segmentations described in Section 2.3.1, similarity matching is performed among deformation time series in the adaptive railway grid. A variety of methods have been proposed for time-series matching, including Euclidean distance [38], correlation-based similarity measures [39], and DTW [40,41]. However, Euclidean and correlation-based methods are sensitive to temporal misalignment and may fail to capture deformation patterns when sequences are not perfectly synchronized. Therefore, DTW is adopted due to its capability to achieve flexible temporal alignment.

To address incomplete observations, a DTW-based Donor–Receptor matching strategy is introduced. Cells containing observations from both ascending and descending orbits constitute the Donor Library, whereas cells containing observations from only one viewing geometry form the Receptor Pool, because their missing complementary LOS component needs to be reconstructed. Let R_i denote the i-th receptor cell and G_j denote the j-th eligible donor cell. Similarity matching between R_i and G_j is performed using the deformation time series from the orbit that is available in both cells, either ascending or descending. Each deformation time series is represented by a sequence of feature vectors derived from the velocity, acceleration, and residual characteristics. For a pair of temporal positions aligned during the DTW procedure, the local weighted distance is defined as:

$$d_{p,q}(R_i,\ G_j) = \sqrt{w_{\mathrm{v}}(\Delta\mu_{\mathrm{vel}})^2 + w_{\mathrm{a}}(\Delta\mu_{\mathrm{acc}})^2 + w_{\mathrm{r}}(\Delta\sigma_{\mathrm{res}})^2} \tag{3}$$

where p and q denote the temporal positions being aligned in the receptor and donor feature sequences, respectively. The terms $\Delta\mu_{\mathrm{vel}}$, $\Delta\mu_{\mathrm{acc}}$, and $\Delta\sigma_{\mathrm{res}}$ represent the differences in the velocity, acceleration, and residual features between the aligned feature vectors of R_i and G_j, respectively. The parameters w_{v}, w_{a}, and w_{r} are the corresponding feature weights.

For each receptor cell R_i, the DTW distances to all eligible donor cells are calculated using the shared viewing geometry. Let $\mathscr{D}_i$ denote the index set of donor cells eligible for receptor R_i:

$$\mathscr{D}_i = \{\, j \mid G_j \text{ is an eligible donor cell for } R_i \}$$

The minimum matching distance is then defined as:

$$D_i^{\min} = \min_{j \in \mathscr{D}_i} D_{ij}^{\mathrm{DTW}} \tag{4}$$

The donor corresponding to $D_i^{\min}$ is selected as the optimal match, and its complementary-orbit observation is used to reconstruct the missing LOS component of R_i. The reconstructed and original LOS observations are then combined to derive vertical and horizontal deformation components.

2.3.3. Reconstruction consistency assessment

To characterize the consistency of reconstructed deformation and to support reconstruction quality screening, a Reconstruction Consistency Index (RCI) is introduced through a normalized mapping of the DTW matching distances. The RCI is a deterministic indicator of the relative consistency between a receptor and its selected donor.

After the optimal donor has been identified for each receptor cell, the cell-specific minimum DTW distances $D_i^{\min}$ are collected across all reconstructed receptor cells. The global minimum and maximum of these distances are denoted by $D_{\min}$ and $D_{\max}$, respectively. To provide a consistent relative measure of reconstruction quality across the study area, each minimum DTW distance is mapped to a RCI as:

$$\mathrm{RCI}_i = C_{\max} - \left(\frac{D_i^{\min} - D_{\min}}{D_{\max} - D_{\min}}\right)\cdot(C_{\max} - C_{\min}) \tag{5}$$

where $C_{\min}$ and $C_{\max}$ define the lower and upper bounds of the index, respectively.

A smaller value of $D_i^{\min}$ indicates greater similarity between the receptor cell and its optimal donor and therefore results in a higher RCI value. Conversely, a larger minimum DTW distance produces a lower RCI value. Therefore, the RCI provides a normalized relative measure of reconstruction uncertainty caused by incomplete dual-orbit observations and the similarity-based donor-matching process. The overall reconstruction, consistency assessment, and two-dimensional decomposition procedure is summarized in Algorithm 1.

2.4. Deformation-based indicators for resilience assessment

In infrastructure resilience assessment, system performance can be represented by different context-dependent measures, depending on the infrastructure type, available data, and assessment objective [42-44]. For railway embankments, deformation behavior provides a structural-performance perspective since excessive settlement, spatially uneven deformation, and changes in deformation rate can affect track geometry stability [45], deformation-related track degradation [46] and serviceability [47,48]. Accordingly, InSAR-derived deformation is used in this study as an observable measure of deformation-related structural performance for resilience assessment.

On this basis, two deformation-based indicators are defined at different temporal scales. The multi-year indicator describes the spatial

Algorithm 1
DTW-based InSAR time-series reconstruction and two-dimensional decomposition.

Input: Raw InSAR LOS data from ascending and descending viewing geometries

Output: Two-dimensional deformation time series (vertical and east-west) and RCI maps
1: Donors $\leftarrow\{G_j:$ observations from both viewing geometries are available$\}$
2: Receptors $\leftarrow\{R_i:$ one viewing geometry is missing$\}$
3: **FOR EACH** $R_i \in$ Receptors **DO**
4: $\mathscr{D}_i \leftarrow \{j : G_j$ is an eligible donor cell for $R_i\}$
5: Compute D_{ij}^{DTW} between R_i and each G_j, $j \in \mathscr{D}_i$
6: $D_i^{\min} \leftarrow \min_{j\in\mathscr{D}_i} D_{ij}^{\mathrm{DTW}}$
7: Best temporal donor $\leftarrow$ the donor cell G_j corresponding to $D_i^{\min}$
8: Nearest opposite-viewing-geometry point $\leftarrow$ find the spatially nearest point associated with the best temporal donor
9: R_i.Missing LOS $\leftarrow$ observed LOS time series of the nearest opposite-viewing-geometry point
10: R_i.Missing geometry $\leftarrow$ satellite geometry of the nearest opposite-viewing-geometry point
11: R_i.Match distance $\leftarrow D_i^{\min}$
12: **END FOR**
13: Receptors.RCI $\leftarrow$ normalize Receptors.Match distance using $C_{\min}$ and $C_{\max}$
14: **FOR EACH** $R_i \in$ Receptors **DO**
15: R_i.Deformation $\leftarrow$ decompose R_i.Observed LOS, R_i.Native geometry, R_i.Missing LOS, and R_i.Missing geometry according to Eq. (2)
16: **END FOR**
17: **RETURN** Receptors.Deformation and Receptors.RCI

variability along railway segments, whereas the event response indicator describes changes in deformation rate and direction relative to the pre-event condition. The two indicators are used to characterize deformation behavior under long-term operational loading and around identified disturbance events.

2.4.1. Multi-year deformation stability metric

Although InSAR enables high-frequency, multi-year deformation monitoring, its measurement precision is generally lower than that of engineering-grade track-geometry inspections, making it difficult to translate individual observations into performance-relevant indicators for resilience assessment. Meanwhile, track geometry inspections provide higher precision but are typically conducted at much lower frequencies. Bridging these complementary characteristics is therefore essential for multi-year railway infrastructure assessment. Metrics such as cumulative settlement [5] and annualized deformation rates [49] offer superior objectivity compared to qualitative assessments and can serve as proxies for deformation-related structural performance over time. However, the deformation magnitude or rate at individual locations does not fully capture the spatial non-uniformity of the deformation field, since variations in deformation change along a railway segment may lead to deformation gradients and differential settlement, thereby contributing to track-geometry deterioration.

To capture this spatial aspect of deformation-related resilience, this paper proposes the Deformation Variability Index (DVI), which is calculated as the standard deviation of annual deformation change within each railway segment. In this context, the DVI represents the multi-year deformation-stability, particularly the capacity to limit the accumulation of spatially non-uniform deformation under persistent loading. DVI does not quantify recovery from a discrete disturbance; rather, it characterizes a chronic stability attribute relevant to resilience. This indicator adopts a segment-based aggregation scale and a standard-deviation formulation conceptually aligned with the Track Quality Index (TQI), which characterizes the spatial variability of track-geometry parameters within a defined track segment, commonly 200 m in length (in EN 13,848–6, [50]). Specifically, for a railway segment k of length L, containing $M_{j,k}$ adjacent cells along a certain railway line j, the DVI is expressed as:

$$\mathrm{DVI}_{j,k}^{u} = \sqrt{\frac{1}{M_{j,k}-1}\sum_{g=1}^{M_{j,k}}\left(v_{j,k,g}^{u} - \bar{v}_{j,k}^{u}\right)^2} \tag{6}$$

$$\mathrm{DVI}_{j,k}^{e} = \sqrt{\frac{1}{M_{j,k}-1}\sum_{g=1}^{M_{j,k}}\left(v_{j,k,g}^{e} - \bar{v}_{j,k}^{e}\right)^2} \tag{7}$$

where $v_{j,k,g}^{u}$ and $v_{j,k,g}^{e}$ denote the vertical and east-west annual deformation rates of cell g within segment k, respectively, and $\bar{v}_{j,k}^{u}$ and $\bar{v}_{j,k}^{e}$ represent the corresponding mean deformation rates across all cells in the same segment. A high DVI indicates high spatial variation in deformation rates within the segment. These processes may have an influence on the deterioration of longitudinal level and alignment. Conversely, a low DVI indicates relatively uniform deformation behavior within the segment. This formulation enables assessment of deformation heterogeneity along the railway while maintaining conceptual consistency with established TG-based indicators.

2.4.2. Event response metric

While the DVI characterizes the multi-year stability of spatial deformation behavior across railway cells, reflecting both spatial consistency and long-term deformation changes under varying operational and environmental conditions, it does not explicitly describe event-scale deformation responses. In the absence of operational-performance or functionality records, the event-scale analysis focuses on changes in the deformation regime relative to the local pre-event baseline. To quantify these responses, an event-centered analysis is applied to the InSAR displacement time series for each cell. For each event, deformation is divided into pre-event, during-event, and post-event phases based on changes in deformation trends rather than nominal event duration.

Specifically, the analysis is centered on the identified event period, with deformation trends examined before and after the event. For the pre- and post-event phases, regression windows are progressively extended from the corresponding event boundaries by incorporating valid observations in order of temporal proximity. The window length is constrained to maintain temporal locality while retaining sufficient observations for trend estimation. Observations that deviate markedly from the local deformation trend are excluded before the final deformation rate is estimated by linear regression [26]. The resulting trends before and after the event-affected period are taken to represent the pre- and post-event phases, respectively. Consequently, the deformation-affected period may extend beyond the nominal event duration, depending on the observed deformation response.

Since deformation rate reflects the temporal evolution of deformation-related performance, comparing the pre-event and post-event slopes provides a proxy for determining the extent to which the post-event deformation regime remains comparable to or departs from

the local pre-event regime. Especially, railway embankments founded on soft clay and peat often exhibit persistent settlement before the occurrence of individual events [5,51]. Therefore, the influence of the event is evaluated based on changes in deformation rate and direction relative to the pre-event condition. An event response ratio R is then defined as the signed ratio between the post-event and pre-event slopes:

$$R = \frac{V_{\text{post}}}{V_{\text{pre}}} \tag{8}$$

R is an event-triggered metric that compares the post-event deformation rate with the pre-event rate. The sign of R indicates whether the pre-event deformation direction is preserved or reversed, while its magnitude indicates whether the post-event deformation rate is attenuated, maintained, or amplified relative to the pre-event condition. Values closer to 1 indicate a smaller event-related effect, with the deformation trend remaining close to its pre-event state. The interpretation of R also considers residual displacement, ground conditions, groundwater variation, and event characteristics.

3. Case study and datasets

3.1. Case study railway section

The studied railway section lies on a railway line in the Netherlands, spanning about 6 km. This section was selected as a case study due to its geotechnical and environmental characteristics, which pose challenges to infrastructure resilience. Geologically, this area is underlain by soft soil strata that exhibit high sensitivity to hydro-meteorological fluctuations, particularly variations in groundwater levels and soil moisture content. The embankment is not only susceptible to multi-year consolidation settlement, but also to seasonal changes triggered by extreme precipitation or drought events. Therefore, the combination of high operational demand and soil-water interactions makes this railway section a suitable case for assessing both multi-year and event-based resilience.

3.2. Remote sensing data

The European Ground Motion Service provides freely accessible displacement time series across Europe derived from Sentinel-1 SAR measurements [52,53]. While Ortho (Level-3) measurements offer pre-calculated 2D displacements, their standardized 100 m resolution [54] often overlooks the fine-scale functional geometry of railway embankments. To preserve the native spatial resolution required for resilience assessment, this paper adopts the Calibrated (Level-2) measurements [55] as the foundational input. This dataset provides dense LOS time series for both ascending and descending geometries, calibrated against GNSS-derived models for absolute geodetic reference. For the case study, C-band Sentinel-1A/B acquisitions from 2018 to 2022 were analyzed. An overview of the datasets is provided in Table 1.

Based on the OpenStreetMap vector data, the railway was transversely segmented into two monitoring zones: a rail zone (0–4.5 m) and an embankment zone (4.5–20.0 m) relative to the centerline. For each independent zone (rail, left embankment, and right embankment), the algorithm iteratively evaluates cell lengths of 5 m, 10 m, 15 m, and 20 m. A cell is considered valid only when it contains sufficient points enabling LOS decomposition. If these conditions are not met even at the maximum cell length of 20 m, the cell is classified as single-geometry or insufficient data. Table 2 summarizes the statistical results of the adaptive grid generation for the case study railway section. The resulting single- and dual-orbit cells are spatially interspersed along the railway section rather than being concentrated in separate segments.

Table 1
Sentinel-1 data employed for processing, including orbit pass, track, and number of acquisitions.

Dataset	First Image	Last Image	Orbit Pass	Track Nr	Acquisitions
1	2018/01/02	2022/12/25	Descending	37	269
2	2018/01/05	2022/12/28	Descending	88	265
3	2018/01/01	2022/12/30	Ascending	110	269
4	2018/01/04	2022/12/21	Ascending	161	269

3.3. Track geometry data

Track geometry variations are inherently linked to the deformation of the supporting substructure, particularly embankment settlement. In practice, it is the spatial variability of settlement that influences the development of track irregularities, as reflected in track geometry measurements. TG measurements serve as a standardized diagnostic tool for assessing railway infrastructure quality, using measurement cars equipped with sensors and instruments [56]. TG data are collected at high spatial resolution and, in the Netherlands, are generally collected four times per year. To quantify rail geometric irregularities, the raw TG measurements are further processed into the TQI, which is calculated as the standard deviation of measured parameters such as the longitudinal level of both rails, alignment of both rails, gauge, and twist.

Based on this complementary relationship, TG data are used as independent in-situ reference information to assess the engineering consistency of satellite-based deformation results. The comparison is conducted separately for vertical and horizontal deformation components. Specifically, longitudinal level in the D1 (3–25 m) and D2 (25–70 m) wavelength ranges is compared with satellite-based vertical settlement, because it is sensitive to differential settlement along the track. TG alignment is compared with the InSAR-derived east-west deformation component to examine whether lateral track-geometry irregularities and satellite-observed horizontal deformation show consistent spatial tendencies. However, because TG and InSAR are based on different measurement principles and may capture different aspects of railway conditions, the comparison is interpreted as complementary evidence rather than direct validation.

3.4. Soil moisture data and extreme event detection

The structural behavior of railway embankments is sensitive to hydro-meteorological conditions, particularly in soft-soil environments [57]. Variations in soil moisture have been recognized as an important environmental factor contributing to embankment deterioration and instability. Therefore, daily surface soil moisture data were acquired from NASA POWER, and extreme hydrological events were identified using percentile-based thresholds of the historical distribution [58]. Specifically, periods in which soil moisture exceeds the 95th percentile (P95) are defined as extreme wet events, while those falling below the 5th percentile (P05) are defined as extreme dry events. Deformation behavior based on these windows was then examined together with TG observations in the following sections. This provides an empirical reference for comparing railway responses under future hydrological conditions and for interpreting more severe deterioration or instability should it occur.

Fig. 3 shows the temporal distribution of extreme hydrological

Table 2
Statistical results of the adaptive grid.

Sort	Number	Proportion	RCI range
Valid cells	274	28.4%	0.95
Cells with single orbit	400	41.5%	0.05–0.95
Cells with no points	291	30.1%	0
Total	965	100%	0–0.95

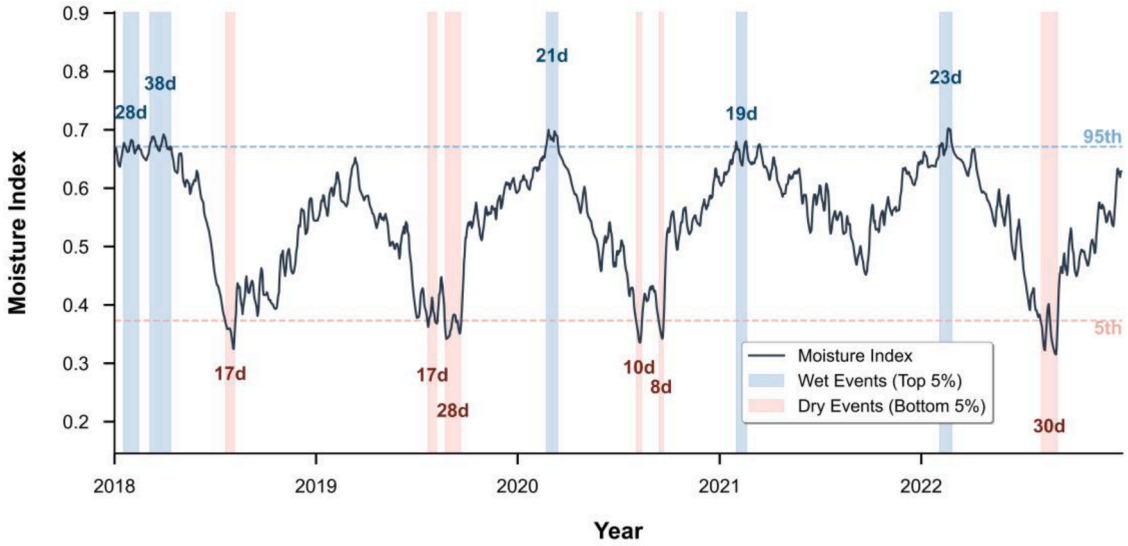


Fig. 3. Extreme soil moisture event detection based on percentile thresholds.

disturbances identified for the event-based resilience assessment. The soil moisture index exhibits high-amplitude fluctuations (0.30–0.70), with the adaptive thresholds (P95≈0.67; P05≈0.37) derived from its own distribution, enabling data-driven identification of local extremes. The detected wet (blue shaded) and dry (yellow shaded) anomalies represent acute hydraulic stressors that deviate significantly from the normal baseline. These discrete events constitute the external loading inputs, defining the specific temporal windows necessary for quantifying the embankment's event-based structural response under extreme environmental conditions.

4. Results and discussion

4.1. Parameter selection and sensitivity analysis

To support parameter selection, a parameter sensitivity analysis was conducted over predefined candidate ranges. For each candidate parameter configuration, DTW-based matching was performed and the most similar donor was identified. Parameter performance was evaluated using the RMSE and MAE between the annual deformation rates of each series and its matched donor. The resulting errors were used to support parameter selection for the present dataset. This procedure provides a repeatable basis for parameter selection, allowing the parameters to be determined according to the characteristics of each dataset.

The parameter search was performed in two stages. The HP filtering parameter (λ) and polynomial degree (p) were first jointly evaluated because they determine the extracted trend and temporal segmentation. The DTW feature weights were then assessed under a non-negative sum-to-one constraint to compare the effects of velocity, acceleration, and residual variability on donor matching. The tested parameter ranges and their purposes are summarized in Table 3.

Table 3
Parameter ranges evaluated in the sensitivity analysis.

Parameter group	Parameter	Candidate values / range
Trend extraction and segmentation	λ	10, 100, 1000
Trend extraction and segmentation	p	7–15
DTW feature weighting	w_v, w_a, w_r	Non-negative triplets sampled at 0.25 intervals and normalized so that they sum up to 1 [Equal-weight baseline: (1/3, 1/3, 1/3)]

The joint sensitivity analysis presented in Table 4 showed that both λ and p affected matching performance. The combination $\lambda = 10$ and $p = 10$ achieved the lowest RMSE and MAE for the high-RCI group, with values of 1.877 and 1.210 mm/yr, respectively. The relative performance of the tested parameter combinations varied across the RCI groups, indicating that a single parameter setting does not necessarily minimize the matching errors for all groups. This combination was therefore selected for the present case study, with greater emphasis placed on the high-RCI group. Such differences in group-wise performance are dataset-dependent and are considered when applying the framework to different datasets.

Using the selected trend-extraction parameters, different DTW feature-weight combinations were further evaluated by comparing the annual deformation rate of each series with that of its matched donor, as shown in Table 5. The results indicate clear differences in matching performance among the high, middle, and low RCI groups under different weighting schemes. The selected weights $(w_v, w_a, w_r) = (0.50, 0.25, 0.25)$ achieved the lowest RMSE and MAE for the high-RCI group. For comparison, the alternative schemes in Table 5 yielded lower errors for the middle- and low-RCI groups but higher errors for the high-RCI group. The selected combination was retained because greater emphasis was placed on the high-RCI group. Overall, the selected λ, p, and feature weights are dataset-specific and should not be interpreted as fixed parameters of the framework.

To further examine the cross-site applicability of the proposed framework, an additional case study was conducted on the southern section of the Erfttalbahn railway line. The studied railway section extends predominantly in the north-south direction and was delineated using the local OSM railway centerline. LOS displacement data were retrieved from the European Ground Motion Service. Following the same spatial partitioning strategy, the corridor was divided into the railway and embankment zones, resulting in 697 cells. The proposed framework was then applied to this dataset, with the relevant parameters independently determined for the German case.

For the German case study, the selected λ and p were 100 and 7, respectively, with the MAE value ranging from 0.695 to 1.089 and the RMSE from 0.891 to 1.494 across the RCI groups, with both error metrics increasing from the high to the low RCI group. These errors were lower than those obtained for the Dutch case, while the preferred parameter settings also differed. This indicates that both the parameter

Table 4
Lambda and degree settings in the case study (mm/yr).

Lambda (λ)	Degree (p)	High RMSE	High MAE	Middle RMSE	Middle MAE	Low RMSE	Low MAE
10	10	**1.877**	**1.210**	3.371	2.605	3.748	2.960
1000	13	1.905	1.311	3.444	2.488	3.669	2.611
100	10	1.939	1.293	3.291	2.619	3.511	2.512
10	8	1.995	1.343	4.035	3.142	4.255	3.217
100	15	2.571	1.770	4.109	3.144	3.599	2.807
10	13	3.236	2.080	3.046	2.198	3.904	2.891
10	15	3.642	2.450	3.335	2.463	4.076	3.205

Table 5
Feature weights settings in the case study (mm/yr).

	w_a	w_r	High RMSE	High MAE	Middle RMSE	Middle MAE	Low RMSE	Low MAE
0.500	0.250	0.250	**1.877**	**1.210**	3.371	2.605	3.748	2.960
0.500	0.500	0.000	2.090	1.598	2.494	1.850	3.281	2.478
1.000	0.000	0.000	2.231	1.642	3.217	2.401	4.604	3.357
1/3	1/3	1/3	2.967	1.913	3.520	2.612	3.795	2.944
0.250	0.250	0.500	3.104	1.998	4.195	3.275	4.366	3.308

settings and reconstruction error levels are site dependent, whereas the same parameter selection and reconstruction procedure can be applied across different study areas.

4.2. Case study reconstruction

To evaluate the proposed framework, a global donor search and time-series reconstruction were performed for cells within the monitoring area along the case study railway section to ensure physically consistent matching. A representative reconstructed target point was selected to illustrate the donor-matching process, as shown in Fig. 4.

As shown in Fig. 4a, the target candidate exhibits a clear multi-year settlement trend, with short-term fluctuations superimposed on the fitted deformation trajectory. The selected reference point shows a

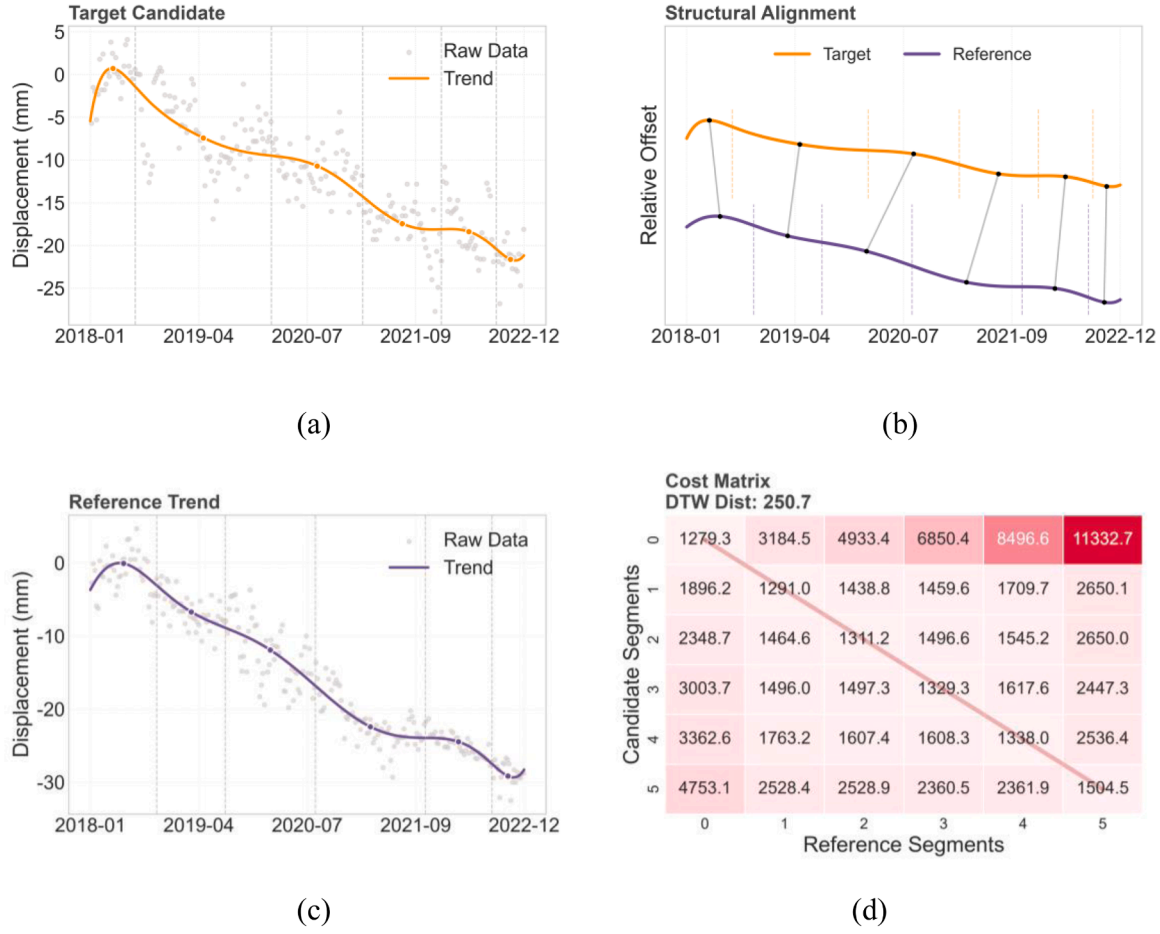


Fig. 4. Representative donor-matching example based on deformation trend and DTW structural alignment: (a) deformation time series and fitted trend of the target candidate; (b) DTW-based structural alignment between the target and reference sequence; (c) deformation time series and fitted trend of the reference sequence; and (d) DTW cumulative cost matrix and optimal alignment path.

broadly similar temporal evolution (Fig. 4c), although its cumulative settlement magnitude is slightly larger than that of the target. To emphasize the similarity in deformation structure rather than absolute displacement magnitude, the two fitted trajectories were compared using relative offsets. The structural alignment in Fig. 4b indicates that the main deformation segments of the target and reference are matched in an approximately one-to-one manner, with only limited temporal shifting between corresponding segments. This is further supported by the DTW cost matrix in Fig. 4d, where the optimal alignment path follows a near-diagonal trajectory and yields a DTW distance of 250.7. The concentration of lower cumulative costs along this path suggests that no substantial temporal reordering or strong non-linear distortion is required to align the two deformation sequences. Overall, the selected reference point captures the main temporal deformation characteristics of the target point, supporting its use for similarity-based reconstruction.

Following the donor selection, Fig. 5 presents the reconstructed LOS time series and the resulting two-dimensional deformation components. The synthesized descending-track LOS series is shown together with the original ascending observations in Fig. 5a, and the two series were subsequently combined to resolve the vertical and east-west deformation components in Fig. 5b. The vertical component exhibits a persistent downward trend over the monitoring period, whereas the east-west component fluctuates and shifts in the positive direction later in the monitoring period.

To evaluate the reconstruction procedure illustrated in Fig. 5, one LOS series was withheld from each cell with complete dual-orbit observations and reconstructed using a different eligible donor. For cells meeting the high-RCI criterion, the reconstructed and observed series were combined to estimate east-west and vertical annual velocities. These velocities were compared with estimates from the complete dual-orbit observations. Table 6 reports the resulting MAE and RMSE with 95% confidence intervals obtained by resampling cells. The vertical component yields lower point estimates for both MAE and RMSE than the east-west component. The confidence intervals overlap for both metrics, indicating that the uncertainty ranges of the reconstruction-error estimates overlap between the two deformation components.

4.3. Multi-year deformation stability assessment

Prior to the vector decomposition, the LOS deformation fields for the ascending and descending orbits were analyzed. Both LOS fields exhibited a dominant negative trend, indicating motion away from the satellite. This pattern suggests a dominant subsidence component, which was subsequently confirmed through vector decomposition.

Table 6
Reconstruction errors for east-west and vertical annual velocities in the high-RCI group.

Velocity component	MAE (mm/yr)	MAE 95% CI	RMSE (mm/yr)	RMSE 95% CI
Vertical	1.305	1.125–1.499	1.702	1.444–1.980
East-west	1.517	1.313–1.738	1.963	1.678–2.251

Following the decomposition, the vertical and east-west displacement components were derived. Statistical analysis revealed an average vertical subsidence rate of −3.7 mm/yr, with a maximum value reaching −11.6 mm/yr. In contrast, the east-west displacement field exhibits a distinct and spatially variable pattern, characterized by both eastward and westward motions with velocities fluctuating from −9.8 to +8.9 mm/yr. Together, these results indicate that the railway is affected by both significant vertical settlement and spatially variable horizontal deformation.

To evaluate the proposed multi-year deformation-stability metric, the analysis examines whether spatially non-uniform settlement, quantified by the spatial standard deviation of InSAR-derived annual deformation rates within each 200 m segment, is associated with faster track geometry deterioration. In other words, the analysis examines whether higher deformation variability is associated with accelerated track geometry deterioration. Railway sections are grouped according to low and high deformation variability, and differences in the annual deterioration rates of TQI are evaluated.

As shown in Fig. 6, sections with higher spatial variability in InSAR-derived annual deformation rates exhibit significantly faster track geometry deterioration. Statistical tests reveal significant differences between vertical deformation variability and both TQI-D1 and TQI-D2 deterioration rates, as well as between east-west deformation variability and TQI-D1 deterioration, where TQI-D1 and TQI-D2 represent track geometry deterioration rates associated with different wavelength bands of the TQI, corresponding to short- and long-wavelength irregularities, respectively. These results demonstrate that deformation heterogeneity, reflecting differential settlement, is closely linked to the rate of track geometry degradation. This relationship supports the use of the DVI as a metric of multi-year deformation stability and as an indicator of a

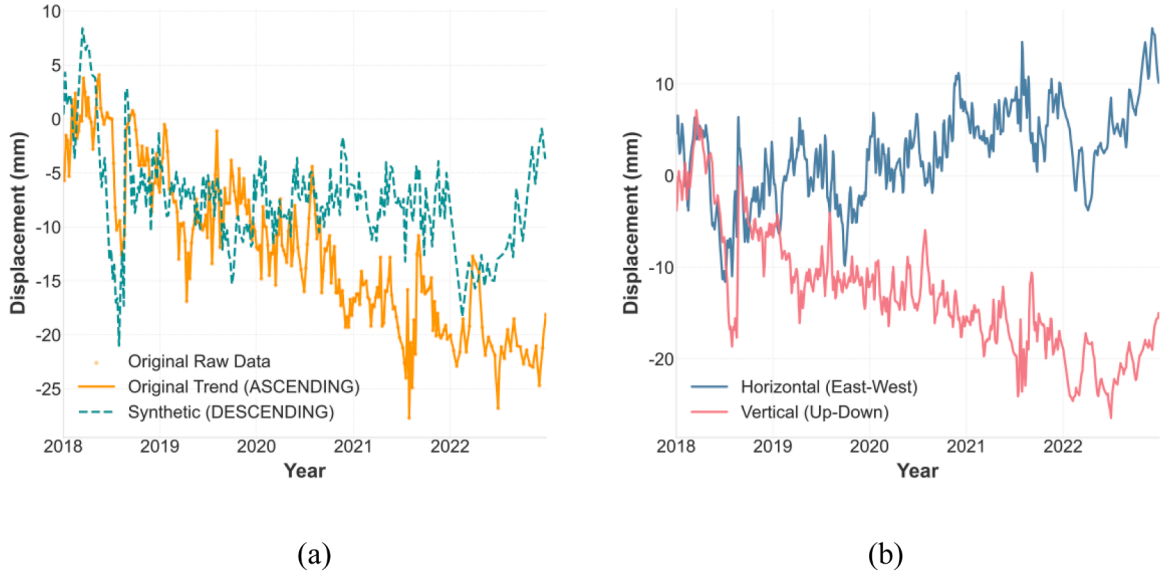


Fig. 5. Time-series reconstruction and 2D deformation decomposition. (a) Original and synthesized LOS time series. (b) Vertical and east-west deformation components.

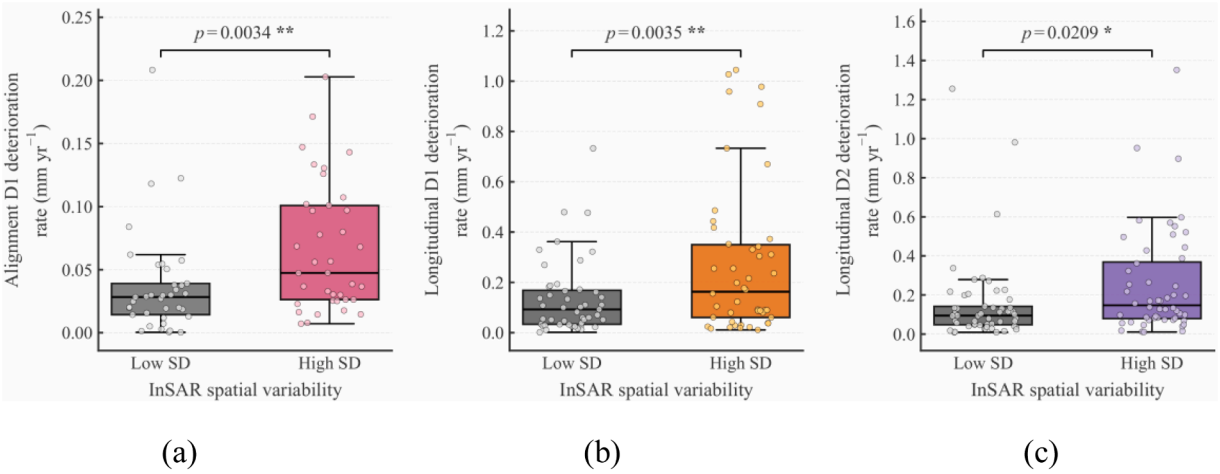


Fig. 6. Relationship between deformation variability and track geometry deterioration (a) Relationship between east-west DVI and the annual deterioration rate of horizontal track geometry (TQI-D1). (b) Relationship between vertical DVI and the annual deterioration rate of vertical track geometry (TQI-D1). (c) Relationship between vertical DVI and the annual deterioration rate of vertical track geometry (TQI-D2).

specific deformation-related dimension of railway infrastructure resilience.

The DVI and conventional TG indicators describe different but related aspects of railway performance. The DVI represents the spatial variability of multi-year deformation rates, whereas TG indicators measure the observed geometric condition of the track. A statistically significant relationship was observed between the DVI and the annual deterioration rates of vertical and horizontal track geometry, supporting the engineering relevance of the DVI as an indicator of sustained deformation-related performance variation. However, this relationship should not be interpreted as a direct linear or one-to-one correspondence.

This lack of direct correspondence is physically reasonable because InSAR and TG measurements represent different physical processes and response mechanisms. InSAR captures continuous deformation of the embankment and track-supporting ground, whereas TG indicators reflect the integrated geometric response of the track structure under train loading, structural transfer, and maintenance interventions. These differences may weaken the direct correspondence between the two measurements. Nevertheless, the segment-based aggregation of adjacent InSAR observations provides some tolerance to minor spatial misalignment, while the use of annualized rates reduces the influence of short-term temporal differences. The observed relationship is therefore interpreted as engineering consistency rather than direct numerical equivalence.

4.4. Event response assessment

Fig. 7 shows an example of an InSAR cell-event used in the event-based deformation response assessment during the identified high-moisture period. The estimated settlement rate changed from −54.5 mm/year before the event to −58.7 mm/year after the event, giving a deformation-based resilience ratio of 1.08 and an RCI of 0.90. This suggests that the post-event deformation rate was slightly higher than the pre-event rate. This example illustrates how the event-based indicators were derived at the cell-event scale.

After calculating the deformation-based resilience ratios for all identified cell-events, the railway cells were ranked according to the deviation of R from the stable value of 1, quantified as $|R-1|$. The upper 5% of cell-events with the largest $|R-1|$ values were defined as alarm cases. In contrast, the 5% of cell-events with $|R-1|$ values closest to 0 were selected as stable cases. Consistent with the cells criterion

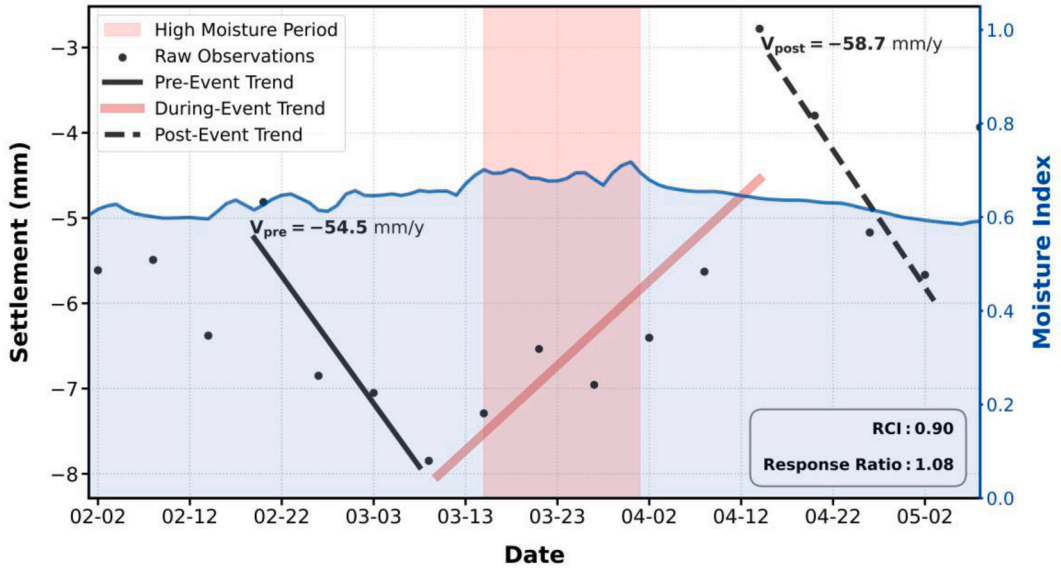


Fig. 7. Illustration of the event response.

adopted in Section 4.1, only cases with high RCI groups were retained for the subsequent TG consistency assessment. Since the RCI filtering was applied after the percentile-based selection, different numbers of high-consistency cases remained in the alarm and stable groups.

Meanwhile, the TG response classification was defined using two thresholds representing the event-associated change. For the case-study section, where the operating speed is greater than 80 km/h and does not exceed 120 km/h, a post-event longitudinal-level standard deviation of 1.80 mm was used as the absolute TG condition threshold, while an increase of 0.70 mm was used to indicate a meaningful before-after change. The former was used to identify cases where the post-event longitudinal-level variability was relatively high, whereas the latter was used to identify cases where the longitudinal-level variability increased noticeably after the event. Together, these two thresholds capture both the absolute post-event TG level and the magnitude of the before-after change (EN 13,848–6 2014; [59]).

Let σ_{pre} and σ_{post} denote the standard deviations of longitudinal level before and after an identified event, respectively, and let $\Delta_\sigma = \sigma_{post} - \sigma_{pre}$. The InSAR-defined groups, corresponding TG response criteria, and TG-consistency rates are summarized in Table 7.

Here, the TG-consistency rate is defined conditionally within each InSAR-selected group. For the InSAR alarm group, it represents the proportion of selected events for which the matched TG observations showed an elevated before-after response, whereas for the stable group, it represents the proportion showing a subtle before-after response. Thus, the TG responses measures how frequently the TG response category was consistent with that expected after an event had already been classified according to the InSAR criterion.

InSAR-derived deformation and TG characterize different dimensions of railway condition and are not expected to exhibit direct pointwise or numerical equivalence. InSAR-derived deformation highlights spatial ground-deformation patterns, whereas TG primarily reflects the geometric response of the track. InSAR may therefore provide additional spatial information on underlying ground behavior that is not directly represented in TG measurements. Previous studies have therefore compared InSAR-detected railway anomalies using spatial correspondence with track inspection measurements and incident records, rather than through direct comparison of measurement magnitudes [60,61]. Accordingly, TG observations were used here as independent engineering evidence to assess the consistency of the selected InSAR cell-events within the predefined temporal and spatial matching criteria. The resulting consistency rate reflects the extent to which the InSAR-selected events are accompanied by corresponding TG responses.

As shown in Table 7, 122 of the 200 alarm InSAR cases (61.0%) were accompanied by an elevated TG response, characterized by either an increase in longitudinal-level variability or a comparatively elevated post-event TG value. For the stable InSAR cases, 143 of 191 cases (74.9%) exhibited a subtle TG response, with TG observations remaining below both response thresholds. These results indicate that a proportion of the InSAR-selected events showed corresponding response levels in an independent monitoring source.

The spatial distributions of the two monitoring results were further examined for the 2020 event period. As shown in Fig. 8, alarm InSAR cells and elevated-response TG segments are presented separately, allowing their spatial correspondence to be visually compared.

The spatial correspondence represented in Fig. 8 was further quantified using a random baseline. Since the raw overlap rate depends on both the number of selected InSAR cells and the spatial extent of elevated-TG segments, the observed correspondence was further evaluated against an event-specific random baseline to account for these differences across events [1]. For each event, the observed number of InSAR alarm cells was retained, while the same number of cells was repeatedly sampled from the available InSAR cells with the TG segments kept fixed. This provided the overlap expected under random cell selection. The observed overlap consistently exceeded this expectation, with observed-to-expected ratios ranging from 1.98 to 2.90. Together, these analyses characterize the InSAR-TG correspondence from both event-wise and spatial-randomization perspectives.

Overall, the event-based comparison showed consistent directional correspondence between the InSAR-derived deformation responses and TG observations, while the randomization analysis further showed that their spatial co-location exceeded that expected from random spatial coincidence. Given the differences in measurement targets and spatial support between the two monitoring sources, these correspondences provide cross-source evidence that the observed spatial associations exceed those expected from random spatial overlap, thereby providing additional information for railway embankment assessment.

4.5. Discussion

The combined results of the multi-year and event-based assessments in the case study highlight their complementary roles in characterizing railway embankment behavior across different temporal scales. They also indicate that InSAR-derived indicators can be interpreted within a deformation-related resilience framework rather than as a complete measure of system-level railway resilience.

The proposed framework is intended as a supplementary assessment and screening tool within a broader railway monitoring pipeline. By integrating multi-year spatial deformation variability with short-term responses, it provides complementary spatial and temporal information for identifying locations that may warrant closer inspection. The resulting indicators are therefore intended to support screening and prioritization rather than directly trigger maintenance actions. Maintenance decisions should continue to rely on established track-geometry criteria, field inspections, and maintenance records.

The event-based analysis focuses on characterizing deformation responses to known extreme hydrological events. The performance of the framework may also be influenced by local geological conditions, satellite point density and temporal coverage, and the proportion of observations requiring reconstruction. Future research should verify its transferability to other railway and environmental settings, develop explicit uncertainty propagation from InSAR observations through reconstruction and subsequent deformation indicators. Building on this, satellite observations could be used to test unsupervised detection of emerging deformation patterns and probabilistic forecasts of threshold exceedance without predefined event windows. These forecasts could support proactive reliability assessment and inform risk-based maintenance planning [62] and decisions under model uncertainty [63].

5. Conclusions

Overall, the results of the case study demonstrate the potential of

Table 7
Event-level correspondence between InSAR-defined groups and TG responses.

Deformation-based InSAR group	InSAR selection criterion	TG response considered consistent	TG criterion	Number of consistent cases	TG-consistency rate
Alarm InSAR cases	Upper 5% of $\lvert R-1\rvert$	Elevated-TG response	$\Delta_\sigma > 0.70$ mm OR $\sigma_{post} > 1.80$ mm	122/200	61.0%
Stable InSAR cases	5% of $\lvert R-1\rvert$ closest to 0	Subtle TG response	$\Delta_\sigma \leq 0.70$ mm AND $\sigma_{post} \leq 1.80$ mm	143/191	74.9%

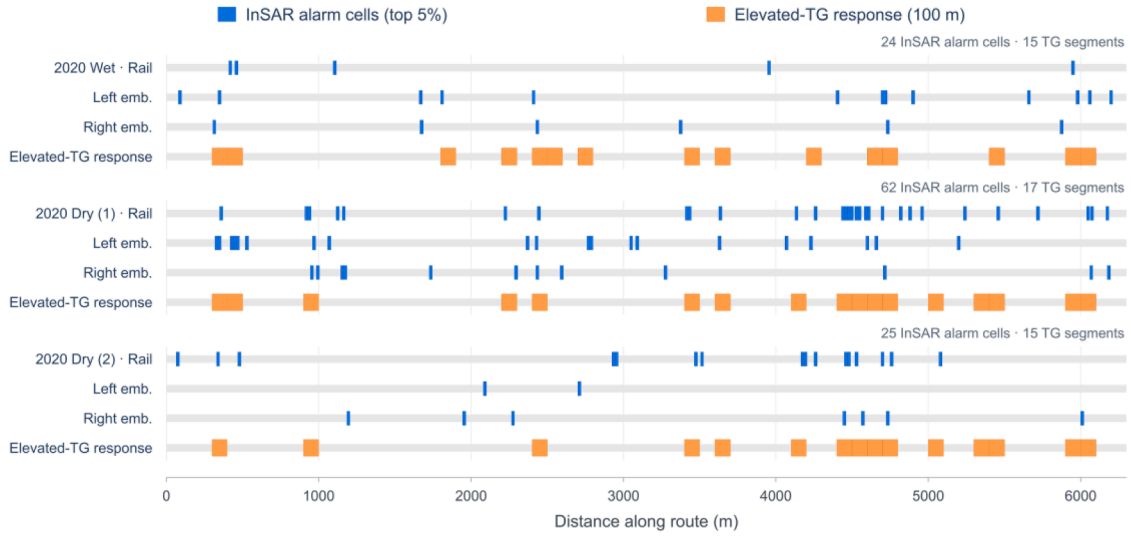


Fig. 8. Spatial comparison between alarm InSAR cells and segments with elevated-response TG during the 2020 event periods.

satellite observations to provide insights into multi-year deformation behavior and event-based responses of railway embankments. Methodologically, the framework combines adaptive spatial cells, LOS-based two-dimensional deformation decomposition, and segment-based reconstruction of missing observations, with reconstruction-related uncertainty considered through the RCI. The reconstructed deformation time series are then translated into two deformation-based indicators within a deformation-related resilience framework, capturing spatial heterogeneity and event-related changes at different temporal scales.

In this case study, higher DVI values, indicating greater spatial heterogeneity in deformation, were associated with greater annual TQI deterioration. For the event-based assessment, 61.0% of the alarm InSAR cases were accompanied by an elevated-TG response, while 74.9% of the stable InSAR cases were accompanied by a subtle TG response. These results provide case-study evidence that satellite-derived indicators can complement conventional railway assessment with more frequent and spatially distributed deformation information. The event-based results should be interpreted as conditional cross-data consistency within predefined disturbance windows, rather than as classification accuracy, event-detection, or forecasting performance.

CRediT authorship contribution statement

Mengyi Wang: Writing – review & editing, Writing – original draft, Visualization, Validation, Methodology. **Hongrui Wang:** Writing – review & editing, Supervision, Methodology, Conceptualization. **Alfredo Núñez:** Writing – review & editing, Supervision, Funding acquisition. **Bart De Schutter:** Writing – review & editing, Supervision.

Declaration of competing interest

The authors declare that they have no known competing financial interests or personal relationships that could have appeared to influence the work reported in this paper.

Acknowledgements

This research was partly supported by ProRail and Europe's Rail Flagship Project IAM4RAIL - Holistic and Integrated Asset Management for Europe's RAIL System under Grant Agreement No 101101966. Funded by the European Union. Views and opinions expressed are however those of the author(s) only and do not necessarily reflect those of the European Union or Europe's Rail Joint Undertaking. Neither the European Union nor the granting authority can be held responsible for them. The project FP3-IAM4Rail is supported by the Europe's Rail Joint Undertaking and its members.

Co-funded by the European Union

Europe's Rail

Data availability

Data will be made available on request.

References

[1] Amaya-Gómez R, Sánchez-Silva M, Muñoz F, Schoefs F, Bastidas-Arteaga E. Spatial characterization and simulation of new defects in corroded pipeline based on in-line inspections. Reliab Eng Syst Saf 2024;241:109697. https://doi.org/10.1016/j.ress.2023.109697.

[2] Kim Y, Carvalhaes T, Helmrich A, Markolf S, Hoff R, Chester M, Li R, Ahmad N. Leveraging SETS resilience capabilities for safe-to-fail infrastructure under climate change. Curr Opin Env Sustain 2022;54:101153. https://doi.org/10.1016/j.cosust.2022.101153.

[3] Liang C, Guan M. Increasing flood hazards threaten metro system resilience under climate and demographic changes. Sustain Cities Soc 2025;133:106890. https://doi.org/10.1016/j.scs.2025.106890.

[4] Yun CB, Min J. Smart sensing, monitoring, and damage detection for civil infrastructures. KSCE J Civ Eng 2011;15(1):1–14. https://doi.org/10.1007/s12205-011-0001-y.

[5] Azadnejad S, Hrysiewicz A, Trafford A, O'Loughlin F, Holohan EP, Kelly F, Donohue S. InSAR supported by geophysical and geotechnical information constrains two-dimensional motion of a railway embankment constructed on peat. Eng Geol 2024;333:107493. https://doi.org/10.1016/j.enggeo.2024.107493.

[6] Lu Z, Feng Y, Tang C, Zhao Y, Zhang J, Hu Z. Thermo-hydro-mechanical coupling effects on cyclic dynamic behavior of saturated soft soil. J Rock Mech Geotech Eng 2026;18(7):5829–38. https://doi.org/10.1016/j.jrmge.2025.09.029.

[7] Di Pietro A, Tofani A, Fuggini C, Solari C, Oliva G. An impact risk assessment methodology for the evaluation of the economic, social and operational resilience of critical infrastructures. Int J Disaster Risk Reduct 2026;132:105965. https://doi.org/10.1016/j.ijdrr.2025.105965.

[8] Zhu Y, Zhang Q-B. Lifecycle resilience and sustainability trade-offs for underground infrastructure under multi-hazard scenarios. Reliab Eng Syst Saf 2026;267:111797. https://doi.org/10.1016/j.ress.2025.111797.

[9] Haghighi E, Kasraei A, Famurewa S, Strandberg G, Sas G, Garmabaki A. Climate change risks on railway infrastructure: a systematic review and analysis. Sustain Cities Soc 2025;129:106504. https://doi.org/10.1016/j.scs.2025.106504.

[10] Peduto D, Giangreco C, Venmans AAM. Differential settlements affecting transition zones between bridges and road embankments on soft soils: numerical analysis of

maintenance scenarios by multi-source monitoring data assimilation. Transp Geotech 2020;24:100369. https://doi.org/10.1016/j.trgeo.2020.100369.
[11] Zhu Y, Zheng G, Zhou H, Xia B, Yu X, He Y, Kalumba D. Evaluation of settlement profiles of soft clay under embankments. Comput Geotech 2025;187:107492. https://doi.org/10.1016/j.compgeo.2025.107492.
[12] Tan M, Yang Y, Bian L, Zhang J, Ohno S. Safe operation plan for high-speed rail based on dynamical prediction model of short-term rainfall. KSCE J Civ Eng 2025; 29(4):100058. https://doi.org/10.1016/j.kscej.2024.100058.
[13] Vranešić K, Haladin I. The effects of extreme weather conditions on rail traffic. Transp Res Procedia 2025;91:273–80. https://doi.org/10.1016/j.trpro.2025.10.036.
[14] Gallagher JG, Beddoe RA, Take WA. Quantifying the rate of track subsidence on permafrost by inferring absolute surface profile from track geometry. Transp Geotech 2025;54:101625. https://doi.org/10.1016/j.trgeo.2025.101625.
[15] Zhang H, Chin ZY, Borghesani P, Pitt J, Cholette ME. Evaluation of onboard sensors for track geometry monitoring against conventional track recording measurements. Measurement 2024;229:114354. https://doi.org/10.1016/j.measurement.2024.114354.
[16] Festa D, Novellino A, Hussain E, Bateson L, Casagli N, Confuorto P, Del Soldato M, Raspini F. Unsupervised detection of InSAR time series patterns based on PCA and K-means clustering. Int J Appl Earth Obs Geoinf 2023;118:103276. https://doi.org/10.1016/j.jag.2023.103276.
[17] Koohmishi M, Kaewunruen S, Chang L, Guo Y. Advancing railway track health monitoring: integrating GPR, InSAR and machine learning for enhanced asset management. Autom Constr 2024;162:105378. https://doi.org/10.1016/j.autcon.2024.105378.
[18] Shih DS, Shih S-S, Hsu SM, Lin S-Y, Lin Y, Hung C-T, Wang K. A framework for the sustainable risk assessment of in-river hydraulic structures: a case study of Taiwan's Daan River. J Hydrol 2023;617:129028. https://doi.org/10.1016/j.jhydrol.2022.129028.
[19] Azadnejad S, Esmaeili M, Maghsoudi Y, Donohue S, Khoshlahjeh Azar M. Extending polarimetric optimization of multi-temporal InSAR techniques on dual polarized Sentinel-1 data. Adv Space Res 2023;72(2):349–60. https://doi.org/10.1016/j.asr.2023.03.009.
[20] Luo Q, Li J, Zhang Y. Monitoring subsidence over the planned Jakarta–Bandung (Indonesia) high-speed railway using Sentinel-1 multi-temporal InSAR data. Remote Sens 2022;14(17):4138. https://doi.org/10.3390/rs14174138.
[21] Kulsoom I, Hua W, Hussain S, Chen Q, Khan G, Shihao D. SBAS-InSAR based validated landslide susceptibility mapping along the Karakoram Highway: a case study of Gilgit-Baltistan, Pakistan. Sci Rep 2023;13(1):3344. https://doi.org/10.1038/s41598-023-30009-z.
[22] Haghighi E, Kasraei A, Kumar U, Famurewa S, Garmabaki AHS. Data-driven risk assessment of climate-related failures in railway infrastructure. Sustain Cities Soc 2026;146:107519. https://doi.org/10.1016/j.scs.2026.107519.
[23] Hanssen RF. Data analysis and interpretation for deformation monitoring. Radar Interferom: Data Interpret Error Anal 2001:161–96. https://doi.org/10.1007/0-306-47633-9_5.
[24] Wright TJ, Parsons BE, Lu Z. Toward mapping surface deformation in three dimensions using InSAR. Geophys Res Lett 2004;31(1):L01607. https://doi.org/10.1029/2003GL018827.
[25] Chang L, Dollevoet RPBJ, Hanssen RF. Monitoring line-infrastructure with multisensor SAR interferometry: products and performance assessment metrics. IEEE J Sel Top Appl Earth Obs Remote Sens 2018;11(5):1593–605. https://doi.org/10.1109/JSTARS.2018.2803074.
[26] Caspani VF, Tonelli D, Bado MF, Rocca A, Perissin D, Zonta D. Bridge monitoring with satellite InSAR technology and clustering algorithm. Measurement 2026;258: 118939. https://doi.org/10.1016/j.measurement.2025.118939.
[27] Giordano PF, Kamariotis A, Giardina G, Chatzi E, Limongelli MP. Uncertainty propagation in satellite InSAR data analysis for structural health monitoring. Autom Constr 2025;177:106371. https://doi.org/10.1016/j.autcon.2025.106371.
[28] Zhang Y, Gao Y, Du S, Zhang S, Li S, Duan W, Prieto JF, Fernández J. 3D surface displacement modeling in Lorca, Spain, using dual-orbit MT-InSAR and multiple prior constraints. Int J Appl Earth Obs Geoinf 2025;145:104967. https://doi.org/10.1016/j.jag.2025.104967.
[29] Bagnall A, Lines J, Bostrom A, Large J, Keogh E. The great time series classification bake off: a review and experimental evaluation of recent algorithmic advances. *Data* Min *Knowl Discov* 2017;31(3):606–60. https://doi.org/10.1007/s10618-016-0483-9.
[30] Zhang J, Wang P, Wang W. Online state recognition of streaming time series based on subsequence similarity. Inf Sci 2026;735:123082. https://doi.org/10.1016/j.ins.2026.123082.
[31] Cao Z, Yang Z, Zhou C, Li Z. Frequently updating DEMs based on multi-track repeat-pass InSAR observations using robust variance component estimation. Int J Appl Earth Obs Geoinf 2025;143:104821. https://doi.org/10.1016/j.jag.2025.104821.
[32] Rahardja D. Statistical methodological review for time-series data. J Stat Manag Syst 2020;23(8):1445–61. https://doi.org/10.1080/09720510.2020.1727618.
[33] Arij N, Latifi H, Fakhri A, Esmaili R. Four decades of spatio-temporal trends in Miankaleh Wetland's water body and vegetation as revealed by remote sensing time series. Ecol Inf 2025;91:103374. https://doi.org/10.1016/j.ecoinf.2025.103374.
[34] Balakrishnan S, Zhang Z, Machemehl R, Murphy MR. Mapping resilience of Houston freeway network during Hurricane Harvey using extreme travel time metrics. Int J Disaster Risk Reduct 2020;47:101565. https://doi.org/10.1016/j.ijdrr.2020.101565.
[35] Pedersen TM. The Hodrick-Prescott filter, the Slutzky effect, and the distortionary effect of filters. J Econ Dyn Control 2001;25(8):1081–101. https://doi.org/10.1016/S0165-1889(99)00059-7.
[36] Wu C, Yu B. Trend-aware time series clustering via self-attentive LSTM. Pattern Recognit 2026;172:112455. https://doi.org/10.1016/j.patcog.2025.112455.
[37] Yu B, Wu C. Fuzzy clustering of time series based on trend feature information granulation. Fuzzy Sets Syst 2025;519:109522. https://doi.org/10.1016/j.fss.2025.109522.
[38] Cheng L, Zhu P, Sun W, Han Z, Tang K, Cui X. Time series classification by euclidean distance-based visibility graph. Phys A: Stat Mech Appl 2023;625: 129010. https://doi.org/10.1016/j.physa.2023.129010.
[39] Li P, Jia R, Cao G, Ming B, Guo Y, Wang S, Li W. A novel perspective for equivalent aggregation of wind farm: measuring the dynamic similarity between output time-series. Appl Energy 2025;392:125958. https://doi.org/10.1016/j.apenergy.2025.125958.
[40] El Amouri H, Lampert T, Gançarski P, Mallet C. Constrained DTW preserving shapelets for explainable time-series clustering. Pattern Recognit 2023;143: 109804. https://doi.org/10.1016/j.patcog.2023.109804.
[41] Glock A-C, Chmelina K, Fürnkranz J, Hütter T. Dynamic time warping for classifying long-term trends in time series. Data Knowl Eng 2026;161:102495. https://doi.org/10.1016/j.datak.2025.102495.
[42] Cimellaro GP, Reinhorn AM, Bruneau M. Framework for analytical quantification of disaster resilience. Eng Struct 2010;32(11):3639–49. https://doi.org/10.1016/j.engstruct.2010.08.008.
[43] Poulin C, Kane MB. Infrastructure resilience curves: performance measures and summary metrics. Reliab Eng Syst Saf 2021;216:107926. https://doi.org/10.1016/j.ress.2021.107926.
[44] Wei Y, Yang X, Xiao X, Ma Z, Zhu T, Dou F, Wu J, Chen A, Gao Z. Understanding the resilience of urban rail transit: concepts, reviews, and trends. Engineering 2024;41:7–18. https://doi.org/10.1016/j.eng.2024.01.022.
[45] Kaewunruen S, Chiengson C. Railway track inspection and maintenance priorities due to dynamic coupling effects of dipped rails and differential track settlements. Eng Fail Anal 2018;93:157–71. https://doi.org/10.1016/j.engfailanal.2018.07.009.
[46] Chiachío J, Chiachío M, Prescott D, Andrews J. A knowledge-based prognostics framework for railway track geometry degradation. Reliab Eng Syst Saf 2019;181: 127–41. https://doi.org/10.1016/j.ress.2018.07.004.
[47] Offenbacher S, Neuhold J, Veit P, Landgraf M. Analyzing major track quality indices and introducing a universally applicable TQI. Appl Sci 2020;10(23):8490. https://doi.org/10.3390/app10238490.
[48] Rempelos G, Ognibene G, Le Pen L, Blainey S, Preston J, Powrie W. Railway track deterioration models: a review of the state of the art. Transp Geotech 2024;49: 101377. https://doi.org/10.1016/j.trgeo.2024.101377.
[49] Wang Y, Dong J, Zhang L, Deng S, Zhang G, Liao M, Gong J. Automatic detection and update of landslide inventory before and after impoundments at the Lianghekou reservoir using Sentinel-1 InSAR. Int J Appl Earth Obs Geoinf 2023; 118:103224. https://doi.org/10.1016/j.jag.2023.103224.
[50] EN 13848-6:2026. Railway applications-track-track geometry quality-part 6: characterization of track geometry quality. Eur Comm Stand 2026. https://www.nen.nl/en/nen-en-13848-6-2026-en-355026.
[51] Peduto D, Huber M, Speranza G, van Ruijven J, Cascini L. DInSAR data assimilation for settlement prediction: case study of a railway embankment in the Netherlands. Can Geotech J 2017;54(4):502–17. https://doi.org/10.1139/cgj-2016-0425.
[52] Ferretti A, Fumagalli A, Novali F, Prati C, Rocca F, Rucci A. A new algorithm for processing interferometric data-stacks: squeeSAR. IEEE Trans Geosci Remote Sens 2011;49(9):3460–70. https://doi.org/10.1109/TGRS.2011.2124465.
[53] Massonnet D, Rossi M, Carmona C, Adragna F, Peltzer G, Feigl K, Rabaute T. The displacement field of the Landers earthquake mapped by radar interferometry. Nature 1993;364(6433):138–42. https://doi.org/10.1038/364138a0.
[54] Crosetto M, Crippa B, Mróz M, Cuevas-González M, Shahbazi S. Applications based on EGMS products: a review. Remote Sens Appl: Soc Environ 2025;37:101452. https://doi.org/10.1016/j.rsase.2025.101452.
[55] Walczak S, Witkowski WT, Stoch T, Guzy A. Detecting sinkholes and land surface movement in post-mining regions using multi-source remote sensing data. Remote Sens Appl: Soc Environ 2025;38:101560. https://doi.org/10.1016/j.rsase.2025.101560.
[56] Phusakulkajorn W, Unsiwilai S, Chang L, Li Z, Núñez A. A hybrid neural model approach for health assessment of railway transition zones with multiple data sources. IEEE Trans Instrum Meas 2025;74:3544017. https://doi.org/10.1109/TIM.2025.3575986. Article.
[57] Khan Q, Saqlain M, Trafford A, Dashwood B, Chambers JE, Jessamy G, Harms J, Donohue S. A combined field and laboratory investigation into the moisture dependency of V_s for a clay-rich railway embankment fill. Eng Geol 2026;367: 108702. https://doi.org/10.1016/j.enggeo.2026.108702.
[58] Azargoshasbi R, Esfeh MA, Kattan L. Urban road network resilience assessment framework: integrating spatiotemporal analysis with the resilience triangle and temporal performance indicators. Reliab Eng Syst Saf 2026;266:111742. https://doi.org/10.1016/j.ress.2025.111742.
[59] Bezin Y, Funfschilling C, Kraft S, Mazzola L. Virtual testing environment tools for railway vehicle certification. Proc Inst Mech Eng F: J Rail Rapid Transit 2015;229 (6):755–69. https://doi.org/10.1177/0954409715587596.

[60] Carlvik F, Mirzanamadi R, Torstensson PT, Eriksson LEB, Göransson G, Palmqvist C-W. Remote sensing of track degradation using InSAR – a case study of the Iron ore line. Transp Res Procedia 2025;86:313–20. https://doi.org/10.1016/j.trpro.2025.04.040.

[61] Ponziani F, Ciuffi P, Bayer B, Berni N, Franceschini S, Simoni A. Regional-scale InSAR investigation and landslide early warning thresholds in Umbria, Italy. Eng Geol 2023;327:107352. https://doi.org/10.1016/j.enggeo.2023.107352.

[62] Consilvio A, Febbraro AD, Sacco N. A rolling-horizon approach for predictive maintenance planning to reduce the risk of rail service disruptions. IEEE Trans Reliab 2021;70(3):875–86. https://doi.org/10.1109/TR.2020.3007504.

[63] Arcieri G, Hoelzl C, Schwery O, Straub D, Papakonstantinou KG, Chatzi E. Bridging POMDPs and bayesian decision making for robust maintenance planning under model uncertainty: an application to railway systems. Reliab Eng Syst Saf 2023;239:109496. https://doi.org/10.1016/j.ress.2023.109496.